Influence of surface texturing on hydrodynamic friction in plane converging bearings – An experimental and numerical approach

Andreas Rosenkranz[1, 2]*, Henara L. Costa[3], Francisco Profito[4], Carsten Gachot[5], Simon Medina[5] and Daniele Dini[6]

[1] Department of Chemical Engineering, Biotechnology and Materials, Universidad de Chile, Santiago de Chile, Chile
[2] Chair for Functional Materials, Department of Materials Science and Engineering, Saarland University, Saarbrücken, Germany
[3] School of Engineering, Universidade Federal de Rio Grande, Campus Carreiros, 96203 900 Rio Grande, RS, Brazil
[4] Department of Mechanical Engineering, Laboratory of Surface Phenomena (LFS), Polytechnic School of the University of São Paulo, São Paulo, Brazil
[5] Institute for Engineering Design and Logistics Engineering, Tribology Research Group, TU Wien, 1060 Vienna, Austria
[6] Department of Mechanical Engineering, Imperial College London, United Kingdom
* Corresponding author: Andreas Rosenkranz, PhD, email: arosenkranz@ing.uchile.cl

Keywords: Hydrodynamic lubrication; surface texturing; ultra-short pulse laser processing; oil film thickness; laser induced fluorescence

Abstract

The frictional behaviour of plane converging bearings was experimentally and numerically studied for four texture geometries fabricated by ultra-short pulse laser texturing (single pocket, line-, cross- and dot-like texture) and convergence ratios under full-film lubrication in the presence of thick oil films (up to 100 µm). Regarding the experiments, small variations in the spread of results between different textures and a general improvement over the untextured reference can be observed. Numerical simulations help to clarify the expected variations and conditions under which these occur. For high convergences, the simulations

demonstrated that textures are beneficial for friction reduction, regardless of load and relative texture's position. For low convergences, a significant friction reduction occurs for textures being located at the bearing's inlet.

1. Introduction

Surface texturing, through the use of regular patterns of protrusions or dimples, has become increasingly used to improve the tribological performance of surfaces in a range of applications including mechanical components in the engine and transmission systems in automobiles [1-3]. One of the origins/inspirations for surface texturing stems from the observations of surface topography changes during "running-in" under mixed lubrication and the subsequent development of optimal surface topography for IC engine piston components. The analysis of worn surfaces shows that wear normally removes the asperity peaks, generating a surface topography consisting of areas of plateaus with truncated asperities and a crosshatch pattern of valleys [4, 5]. The potential for surface texturing to improve the tribological performance and shorten the running-in time of components has therefore been of great interest, particularly for the production of engine components [2-5].

The use of surface texturing to improve the lubrication conditions and to reduce friction and wear between moving parts has also been inspired by studies of the effect of surface topography on hydrodynamic lubrication in face seals. Hamilton et al. and Anno et al. found evidence of the effect of surface irregularities on lubrication [6, 7]. They showed that the use of micro-asperities is an effective and controllable technique for obtaining good hydrodynamic operation in face seals. For conditions involving full-film lubrication, the oil film is typically larger than the heights of the surface asperities [8]. The understanding of the

underlying mechanisms requires examining the hydrodynamic effect that occurs due the presence of a converging wedge [8]. The pockets in a textured surface can act as micro-wedges and therefore contribute to increase the hydrodynamic pressure, with a possible contribution to hydrodynamic lift. However, if the trailing edge of the pocket is considered to act as a converging wedge, then the leading edge of the pocket acts as a (detrimental) diverging wedge. Nevertheless, the occurrence of cavitation still allows for the possibility of a positive net increase due to the presence of the texture, where the increase of pressure at the trailing edge can be higher than the decrease of pressure at the leading edge of the pocket [6, 9-11].

Recently published review articles by Gropper et al. [11] and Gachot et al. [12] provide a detailed summary about the effect of surface texturing under different lubricated conditions. As pointed out by both review articles, considerable experimental and numerical effort has been put to study the influence of different texture parameters such as area density, width and depth and various geometries including closed pockets, chevrons and lines on friction under full-film hydrodynamic lubrication [11, 12]. Regarding the area density, surface textures with area densities between 10 and 30 % have demonstrated beneficial effects [12]. Related to the texture's depth, the interconnection between the oil film thickness and depth has to be considered [13].

Experimentally, Costa and Hutchings measured a small increase in film thickness under full-film lubrication (using capacitance measurements) due to surface texturing, but no detectable effect on friction forces was found [14]. They also proposed the use of textures containing interrupted lines, such as chevron-like features, and showed the importance of the orientation between those and the sliding direction. Vladescu et al. used an optical technique based upon laser induced fluorescence (LIF), which measures the photo-excitation of a fluorescent dye,

adapted to conformal contacts [15]. This set-up allowed them to obtain images of cavitation in the contact. The results showed that under full-film conditions the coefficient of friction (COF) increased with surface texturing. The images showed that when a pocket emerges from the cavitated region, it transfers fluid back into this region, increasing lubricant shear. The authors proposed that this may be responsible for the increase in friction observed for the textured surfaces under full-film lubrication. Recently, ultra-thin optical interferometry was adapted into the same rig, allowing for a precise assessment of the impact of surface texturing on film thickness [16]. Under full-film conditions, surface texturing was again shown to increase the COF. The simultaneous and precise assessment of film thickness and friction also demonstrated that under these conditions film thickness reduced with surface texturing. Thinner films lead to higher shear rates, thus increasing friction. The authors claim that under full-film lubrication surface texturing can increase the COF, although it does boost lubricant entrainment, enabling the transition between mixed and full-film lubrication to occur at lower speeds. Lu et al. used laser surface texturing to fabricate square and triangular textures with different depth profiles to investigate effects coming from converging and diverging texture's characteristics [17, 18]. They demonstrated that the depth profile has a significant effect on the resulting frictional response. Using converging and diverging characteristics, an anisotropic frictional response is induced with lower overall frictional values for the converging geometry.

Numerically, solutions of the 2-dimensional form of the Reynolds equation have been developed to analyse the effects of laser surface texturing on the friction between piston rings and cylinders [19, 20]. More recently, inertial effects have been included in the analysis using mass-conserving algorithms that better represent the film behaviour under conditions of partial cavitation [13, 21-23]. These works have claimed a more realistic account of the

benefits that can be obtained by surface texturing [23], which have been overestimated by algorithms neglecting inertia effects. However, even with the use of mass-conserving algorithms, positive effects of surface texturing have been predicted under certain conditions. For example, Checo et al. have estimated friction reductions up to 73 % and increase in film thickness up to 86 % due to surface texturing [24]. Other similar works have shown that, for large area coverages, intense cavitation reduces film thickness and deteriorates the bearing performance [13, 22], but that for one single large pocket (corresponding to an area coverage of 100 %), cavitation does not develop, so that the best performance is obtained [13, 22, 25]. Codrignani et al. experimentally and numerically investigated the influence of texture shape and position on the frictional response in a macroscopic contact under different lubricated conditions [26]. Under hydrodynamic lubrication, the texture position (front or rear) did not influence the resulting frictional response. They emphasized the need to perform the numerical analysis based upon realistic 2-dimensional surfaces since the results coming from a 1-dimensional solution may be misleading. Moreover, Codrignani et al. demonstrated that the optimal texture's depth scales with the gap height (film thickness), implying that surface textures with a larger structural depth are expected to induce beneficial frictional effects for larger gaps (thicker oil films).

In the present work, complementary experimental and numerical approaches were used to further investigate the behaviour of textured surfaces under thick, full-film lubrication (oil film thickness up to 100 µm). Friction behaviour and oil film thickness of textured plane converging bearings were experimentally studied for different convergence ratios. Different texture geometries (single pocket, dot-, line- and cross-like texture) were produced by ultra-short pulse laser processing in flat silicon substrates. This technique combined with the use of silicon results in ultra-smooth bearing surfaces with well-defined texture features that are

analogous to the idealised geometries represented in the numerical simulations. The numerical simulations were based upon the solution of the Reynolds equation considering the $p-\theta$ Elrod-Adams mass-conserving cavitation model. The simulations provided numerical predictions of the film thickness and COF as a function of the convergence ratio. The goal of the numerical simulations was to achieve a deeper understanding of the underlying mechanisms that affect the frictional performance for the used experimental conditions. They also help to predict the magnitude of changes that may be expected from the experiments and identify the conditions under which such changes tend to occur.

2. Experimental section

2.1 Material

The textured bearing surfaces were made from commercially available (100)-oriented p-type silicon wafers (diameter = 4'', thickness = 300 µm) with a purity of 99.95 %. The surface of the silicon wafer was highly polished, and therefore represented an almost ideally flat surface. Silicon was chosen due to its good surface quality and low surface roughness that ensures planarity of the samples and reproducibility of the experiments as well as avoiding any undesired side effects that may come from rims or bulges, or from bending of the sample. This was necessary to prevent any influence on pressure generation from additional localised convergence/divergence. The uniform and reflective surface was also beneficial for the accuracy and resolution of the LIF technique used to measure film thickness. The silicon wafers were bonded onto thicker steel substrates and the surface profile was measured using white light interferometry (WLI) to ensure the evenness of the samples, prior to laser surface texturing. Silicon samples having a height deviation of less than 1 µm over the entire scan

length (20 mm) were selected for surface texturing and the subsequent tribological experiments.

2.2 Ultra-short pulse laser processing

Four different texture geometries (single pocket, line-like, cross-like and dot-like texture) were selected for the study and are shown in **Figure 1**.

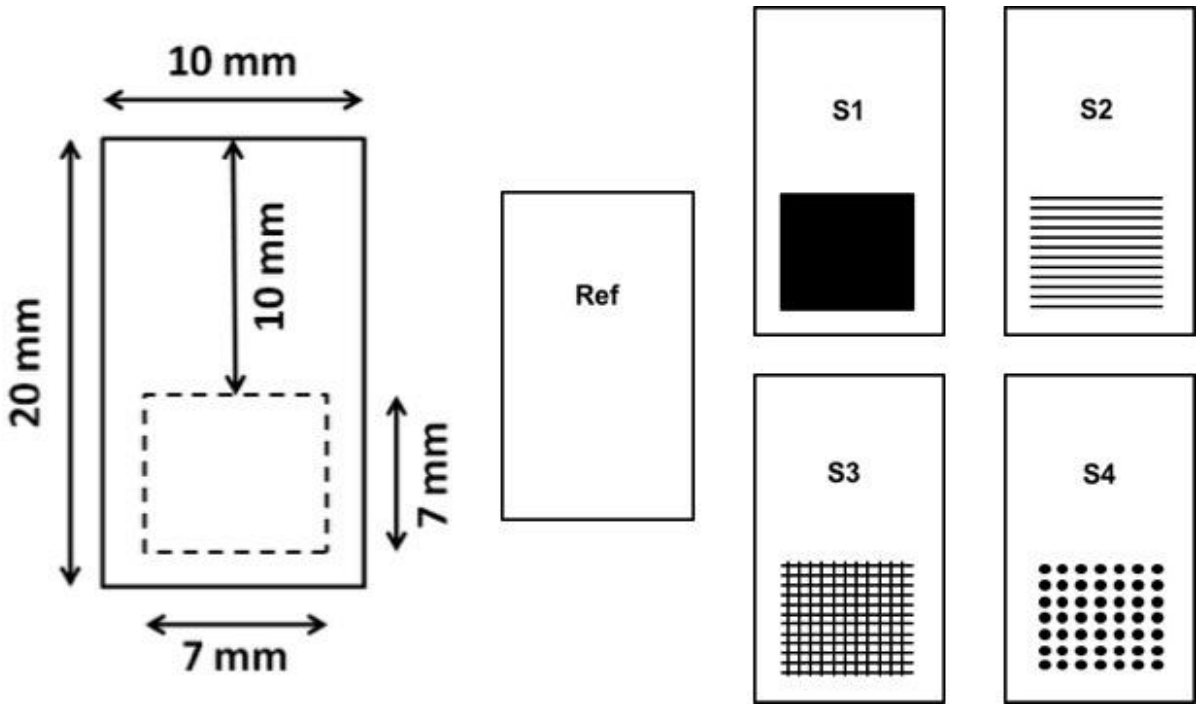

Figure 1: Summary of the idealized texture geometries used in this study. As a reference (ref), an ideally flat silicon surface was used. Four different texture geometries, namely line-, cross- and dot-like texture and a single pocket, were fabricated by ultra-short pulse laser processing. The abbreviation "S1" represents the large single pocket, "S2" stands for the line-like texture, "S3" denotes the cross-like texture and "S4" indicates the dot-like texture.

As can be seen, all textured samples (20 x 10 mm²) have the same nominal textured area of 7 x 7 mm². The large single pocket (S1) was selected due to it sharing similar features to a

Rayleigh step. In addition, it can be considered as a good baseline for comparison with the large pocket densities adopted in the investigation. Theoretically, this texture geometry should present the best tribological behaviour in terms of oil film thickness and load support [27]. The other texture geometries can often be found in the literature and may induce different tribological effects such as an additional hydrodynamic pressure build-up, an enhanced lubricant entrainment or side leakage depending on the respective geometry [13, 22, 28-33].

In order to fabricate the different texture geometries, a passively mode-locked Ti:Sa ultra-short pulse laser (Spitfire Newport Spectra Physics) with a repetition rate of 1 kHz and a wavelength of 800 nm was used. The pulse duration (full width at half maximum), measured and controlled by autocorrelation, was kept constant at 300 ± 30 fs to ensure the same ablation characteristics for all geometries. The use of ultra-short laser pulses was considered to be beneficial due to negligible heat affected zones and the clean processing, thus avoiding contaminations as well as bulges around the textured areas [34]. Consequently, chemical and microstructural changes induced by the laser texturing can be neglected. The primary beam was focused on the silicon using a lens with a focal length of 6.7 cm. The silicon surface was located at the focal point. The laser system was synchronized with a translation table (x-y-stage). For the fabrication of the line- and cross-like textures, a constant translation velocity of the table of 1 mm/s was used. The laser power was kept constant for all textured samples at 3.6 W. After surface texturing, each sample was inspected via light microscopy (Olympus, BX 60*)* and WLI (Zygo, New View 7300).

2.3 Tribological test rig and testing procedure

The experiments were conducted on a purpose-built test rig that enabled the simultaneous measurement of film thickness, friction force and load. An image and schematic of the test rig are shown in **Figure 2**.

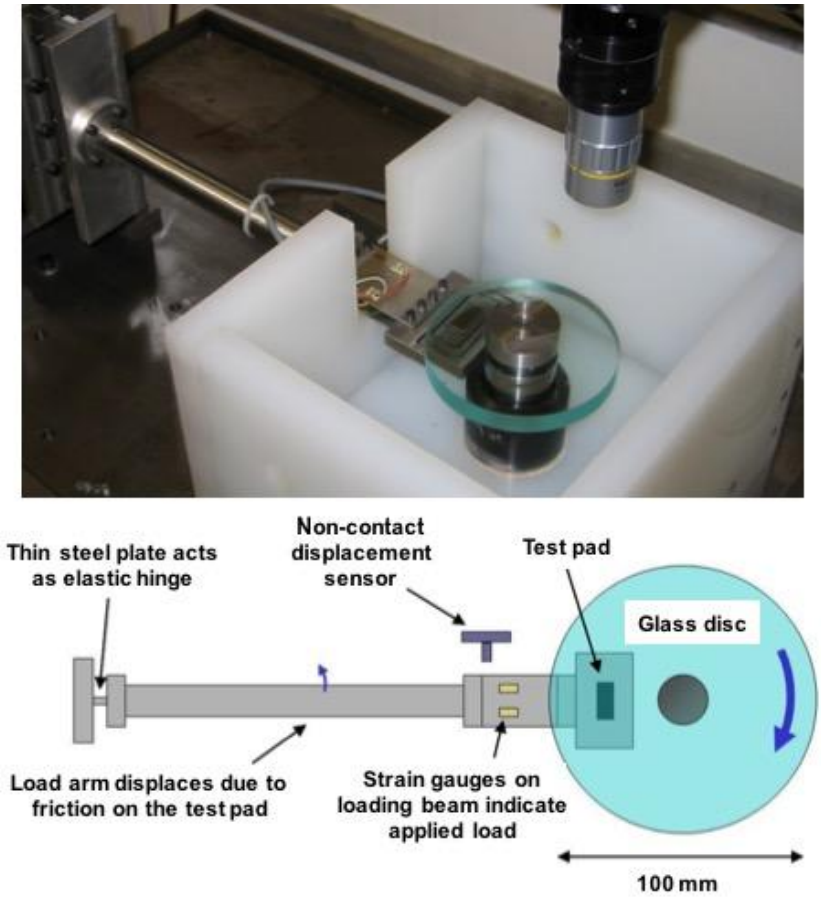

Figure 2: Test rig and loading arm/friction sensing mechanism.

The silicon/steel samples were loaded against a flat, rotating glass disc counter-body. The samples were fixed in a holder located at the end of a loading arm. The normal force was applied by raising the loading arm on a vertical stage, via a twin-leaf spring flexure; the normal load was measured through strain gauges attached to the flexure. In the horizontal

direction, the loading arm was able to pivot about its end and the friction force was determined by small displacements of the load arm, measured by a non-contact displacement sensor near the disc. The stiffness of the pivot was altered to maximise sensitivity of frictional measurements, given the expected range of friction forces and so corresponding displacements. The glass disc was rotated at constant speed to give a sliding velocity of 1.0 m/s at the centre line of the silicon sample, although with this point at a disc radius of approximately 40 mm and a bearing width of 10 mm, a slight variation of the entrainment velocity occurs across the sample.

The holder in which the samples were fixed had a gimbal design that provided independent rotation/alignment parallel and perpendicular to the sliding direction (**Figure 3**).

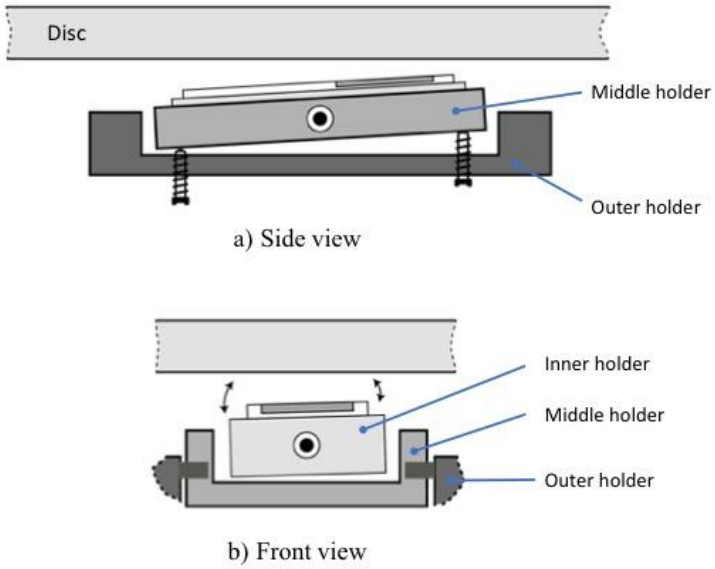

Figure 3: Pad holder. a) Side view showing convergence adjustment screws. b) Front view. Inner holder and sample are free to rotate as indicated.

The samples were free to rotate in the holder about an axis parallel to the sliding (tangential) direction, allowing the silicon surfaces to self-align to the disc surface with respect to the radial direction, i.e. the leading edge of the bearing could align to the disc surface. The attitude angle of the surface in the sliding direction (which determines the overall convergence of the bearing) was fixed by adjusting two screws on the back edge of the sample holder. The attitude angle directly affects the difference in film heights at the inlet and outlet of the bearing and, since the convergence ratio depends on very small changes (on the order of micrometres) to these values, it was impractical to attempt to set a particular convergence. Instead, the angle was adjusted by small amounts between tests, resulting in a range of convergences/attitude angles being tested, and the actual convergence for each test was determined by the film thickness measurements. With the small variation in sliding speed across the inlet, and with some friction in the holder pivot, a small convergence angle perpendicular to entrainment was also expected to occur. Film thickness measurements were made at four points near the pad corners, allowing full assessment of both convergence angles and inlet/outlet film thickness.

To ensure a sufficient oil supply and thus full-film lubrication, the oil was pumped directly onto the glass disc near the inlet, such that there was plentiful oil supply at the bearing inlet but with no additional entrainment provided by the pump.

Film thicknesses (and so convergence ratios) were determined through LIF measurements. With this technique, the intensity of the oil film fluorescence was measured through the glass disc and then converted to a film thickness value via a calibration/correlation process. The LIF set-up used a Mercury UV light source with a 150 W Mercury-Xenon arc lamp with a mono-chromatic filter and controllable shutter. A high sensitivity CCD camera (Rolera MGi) with an objective of 10 x and a zoom of 3 x was used. The oil (Castrol, without any additive)

was mixed with a commercially available oil tracer dye "Dye-Lite", which is a mixture of perylene and naphtalimide, with characteristic fluorescence absorption peaks at 535 and 455 nm, suited to the spectral output peaks of the light source [35].

To calibrate the LIF system, a silicon wedge of known angle was constructed under the glass disc using an identical silicon sample and a glass slip of known height. Prior to each set of experiments, intensity measurements were made along the length of this calibration piece and correlated to the known film thickness. The oil film thickness during the tribological experiment was then obtained from the respective calibration curve acquired prior to the test.

For each test, the temperature of the oil was recorded at the inlet. This temperature varied between 23.5 and 26 °C for all tribological experiments conducted. The temperature-viscosity profile of the oil (including the fluorescent dye) was measured and a value of 150 mPas was used for the numerical simulations.

All experiments were performed at two normal loads, 5 and 10 N, which correspond to nominal contact pressures of 0.025 and 0.05 MPa, respectively. Further information on the rig and details of the experimental set-up can be found in [15].

For each surface texture, tests were performed both with the texture at the front (inlet) of the surface and also at the rear (outlet), as shown in **Figure 4**. Based upon the literature, it is well-known that the position of the textured area with respect to the oil's inlet or outlet can significantly affect the resulting oil film thickness, friction force and load support [13, 36]. As a reference, a plain silicon substrate was used.

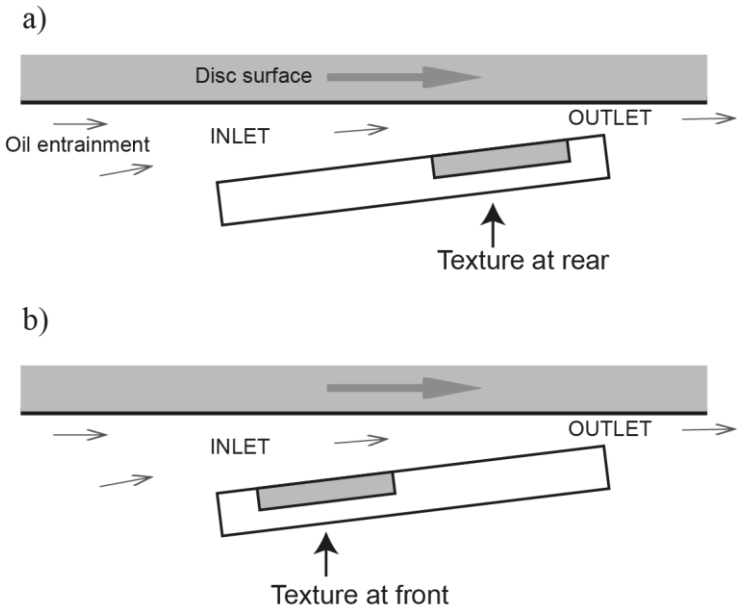

Figure 4: Schematic illustration of the rotating glass disk and the textured silicon substrate depending on the respective texture's position. Texture position configurations: a) Texture at rear (S1r, S2r, S3r and S4r) b) Texture at front (S1f, S2f, S3f and S4f)

2.4 Numerical modelling

This section summarizes the basic mathematical equations and techniques used for the numerical simulations of the textured sliders. The illustration given in **Figure 5** shows a schematic of the set-up used in the numerical model.

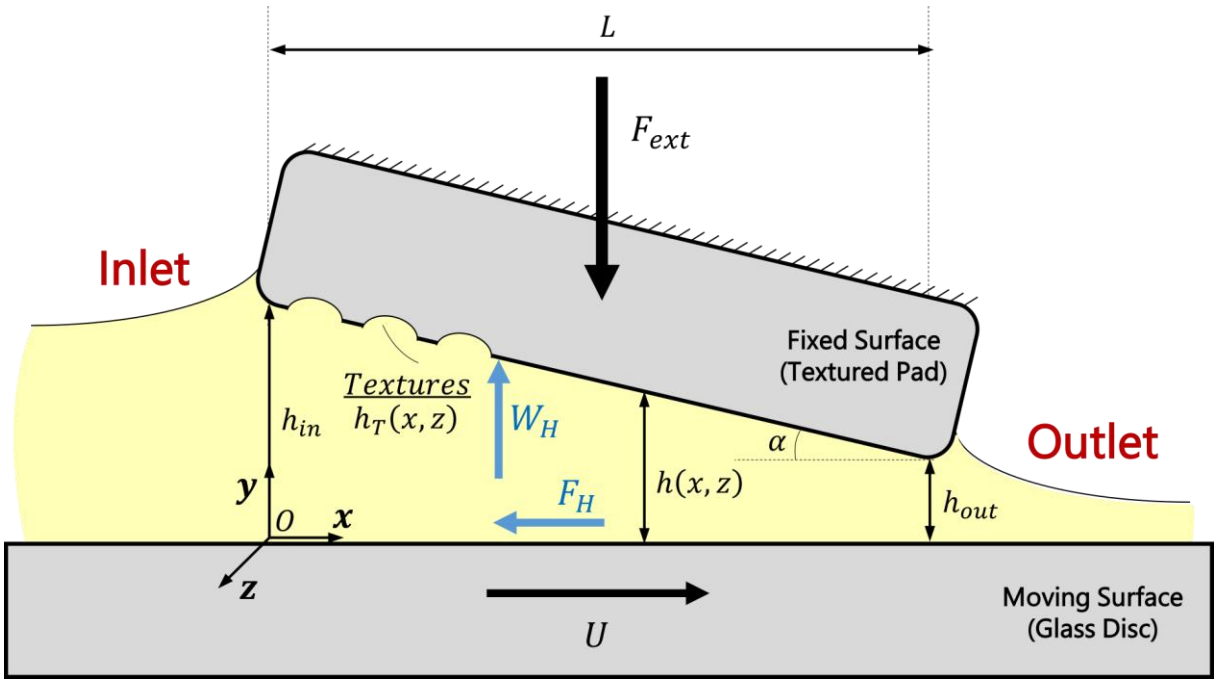

Figure 5: Schematic illustration of the textured slider bearing system showing the main variables and parameters of the mathematical modelling.

The hydrodynamic pressure distribution generated on the textured contact interface was mathematically described through the Reynolds equation considering the $p-\theta$ Elrod-Adams mass-conserving cavitation model [37], which automatically satisfies the complementary JFO conditions for mass-conservation throughout the lubricated domain [38]. In accordance with the system depicted in Figure 5, the transient modified Reynolds equation with $p-\theta$ cavitation model can be expressed as:

$$\frac{\partial}{\partial x}\left[\left(\frac{\rho h^3}{12\mu}\right)\frac{\partial p}{\partial x}\right]+\frac{\partial}{\partial z}\left[\left(\frac{\rho h^3}{12\mu}\right)\frac{\partial p}{\partial z}\right]=\frac{\partial}{\partial x}\left(\frac{\rho U h}{2}\theta\right)+\frac{\partial(\rho h\theta)}{\partial t} \quad (1)$$

Complementary conditions for cavitation:

$$(p-p_{cav})(1-\theta)=0 \;\rightarrow\; \begin{cases} p>p_{cav} \;\rightarrow\; \theta=1 & \text{(pressured regions)} \\ p=p_{cav} \;\rightarrow\; 0\le\theta<1 & \text{(cavitation regions)} \end{cases}$$

where $p(x,z,t)$ is the hydrodynamic pressure, $h(x,z,t)$ the local oil film thickness, U the sliding velocity, μ and ρ the lubricant's dynamic viscosity and density, respectively, and $\theta(x,z,t)$ the film fraction cavitation parameter [39]. The lubricant film thickness can be written in the fixed coordinate system $Oxyz$ as follows:

$$h(x,z,t) = h_{out}(t) + \tan\alpha(L-x) + h_T(x,z), \quad (2)$$

where h_{out} is the oil film thickness at the outlet, α the convergence angle and h_T provides the local texture's depth. The geometric parameters of all textured patterns were identical to the ones used in the experiments. Moreover, in accordance with the conditions used for the tribological experiments, the system is assumed to operate under full-film lubrication. Consequently, no consideration of asperity interactions associated with mixed lubrication was necessary.

The equilibrium equation in the y-direction of the system illustrated in Figure 5 can be written as:

$$W_H(h_{out}) = F_{ext} \;\rightarrow\; \int_{-B/2}^{B/2}\int_{-L/2}^{+L/2}[p(x,z,t)]\,dxdz - F_{ext} = 0, \quad (3)$$

where F_{ext} is the external applied load, W_H is the hydrodynamic load-carrying force produced by the fluid pressure, and B and L are the bearing's length and width, respectively. Similarly, the dissipative viscous friction force (and so the associated COF) can be determined by

$$F_H = \int_{-B/2}^{B/2}\int_{-L/2}^{+L/2}\left(\frac{h}{2}\frac{\partial p}{\partial x} - \frac{\mu U\theta}{h}\right)dxdz, \quad (4)$$

The numerical solution of equation (4) was carried out using a hybrid-type finite volume discretization scheme, namely Finite Volume Method based on Elements, for solving the Reynolds equation with a mass-conserving cavitation model on unstructured meshes [40]. The system of linear equations for p and θ obtained after the discretization process was solved iteratively through a modified Gauss-Seidel method with Successive Over-Relaxation (SOR). Furthermore, the calculation of the minimum oil film thickness that generates the hydrodynamic load capacity necessary to balance the applied external load (F_{ext}) for a given convergence angle (α) was carried out by solving the nonlinear equilibrium equation in y-direction (Eq. 3). The solution of this nonlinear equation was performed using the Newton-Raphson method with Armijo's line search technique [41]. More details about the mathematical modelling and solution framework including its experimental validation and application to transient problems involving textured systems have already been published elsewhere [42, 43].

The method is particularly suited to the analysis of the textures used in this study, since it supports the use of a non-uniform, irregular mesh to define the surface topography. This means that the mesh can be highly refined around the edges of the texture features – providing high accuracy results – but become coarser over the large area of smooth, plane surface – thus reducing computational complexity and solution times.

In order to provide more insights into the experimental findings, numerical simulations were carried out for the same lubricant properties, texture geometries and operating conditions of the experimental tests. **Figure 6** illustrates the finite volume meshes used, which reproduce the geometric features of the fabricated textures shown in Figure 1.

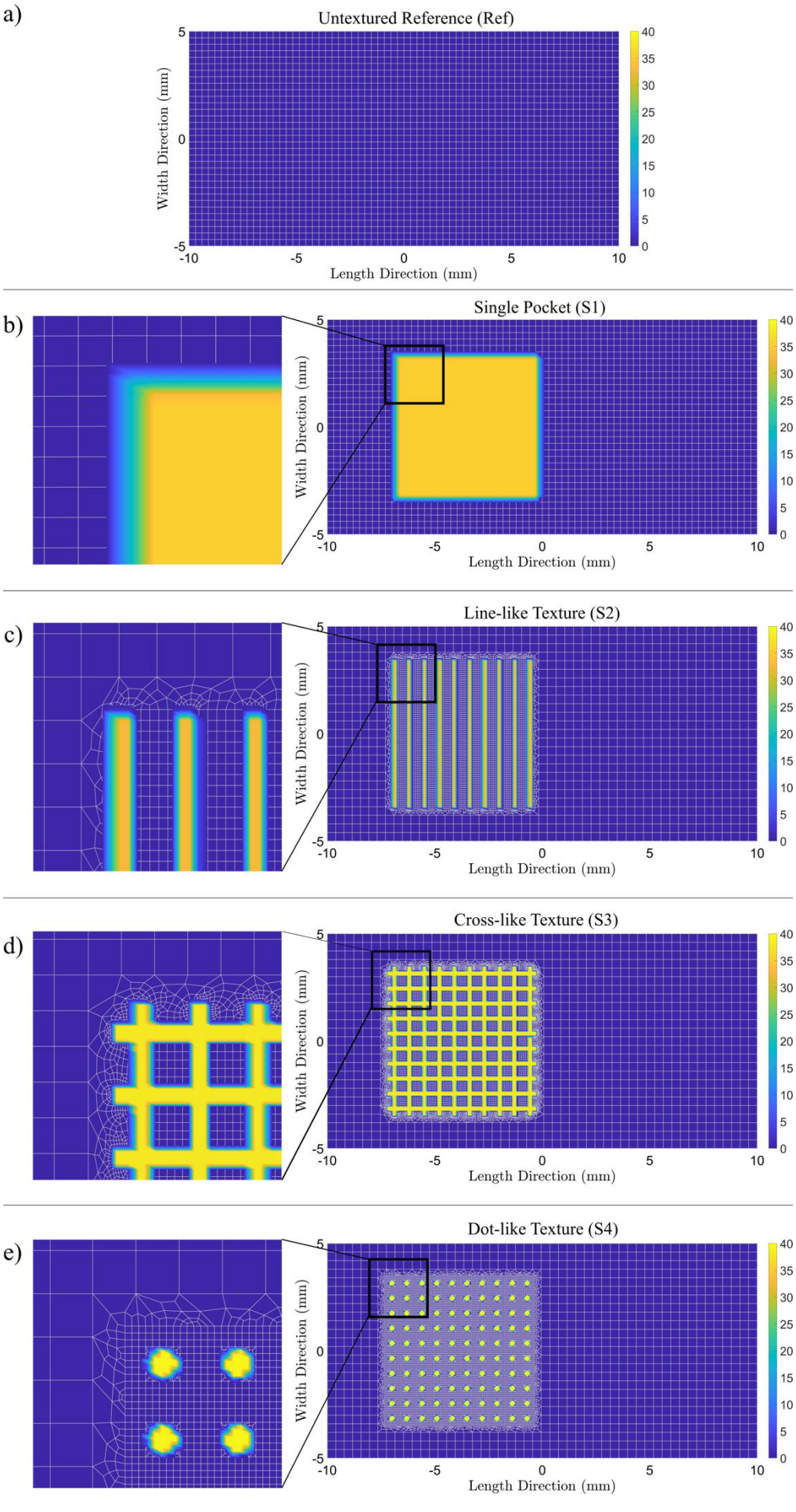
a)
Untextured Reference (Ref)
Width Direction (mm)
Length Direction (mm)
b)
Single Pocket (S1)
c)
Line-like Texture (S2)
d)
Cross-like Texture (S3)
e)
Dot-like Texture (S4)

Figure 6: Finite volume meshes used in the numerical simulations. It is worth to highlight the refinement of the mesh on the textured portions and the presence of unstructured elements in the borders between textured and untextured regions. (a) untextured reference (b) single pocket (S1), 2178 elements; (c) line-like texture (S2), 12073 elements; (d) cross-like texture (S3), 22453 elements; and (e) dot-like texture (S4), 22618 elements. The colour scale represents the respective depth and is given in micrometres. The colour blending at the edges is only a 'graphical artefact' produced by the post-processing visualization tool. In the numerical simulation, sharp transitions were considered at the textures' edges.

The extent of mesh refinements in the proximity of the textures is clear, and is aimed at capturing any influence of the features on the lubrication behaviour, particularly regarding the fluid film cavitation and its effect on the generation of the fluid pressure. The mesh sizes and element distortions were chosen to give a suitable compromise between accuracy and computational cost. The testing conditions, bearing parameter values and lubricant properties used in the simulations are listed in **Table I**.

Table I: Main system parameters, lubricant properties and testing conditions used in the numerical simulations.

Parameter	Value	Unit
Bearing Parameters		
Length	20	mm
Width	10	mm
Lubricant Properties		
Lubricant viscosity	150	mPa.s
Lubricant density	841	kg/m^3
Cavitation pressure	0	Pa
Testing Conditions		
Convergence ratio	0.1 – 15	–

Load	5 and 10	N
Sliding speed	1.0	m/s

3. Results and discussion

3.1 Characterisation of the as-fabricated surface textures

After laser surface texturing, each sample was inspected via light microscopy and WLI. The respective micrographs are shown in **Figure 7**.

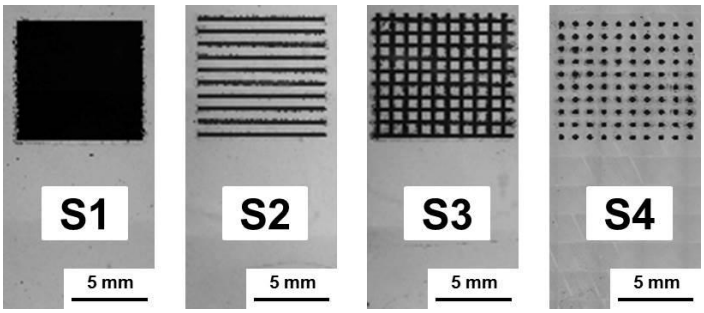

Figure 7: Fabricated texture geometries using ultra-short pulse laser processing measured by light microscopy. It is important to note that, after surface texturing, no polishing process was needed to remove bulges or rims due to the underlying laser-matter interaction.

The depth, periodicity and diameter of the surface textures measured by WLI are summarized in **Table II**.

Table II: Summary of the characteristic texture parameters such as periodicity, width, depth, area density and pocket volume for all produced texture geometries measured by WLI. The area density is normalized to the entire area of the sample (20 mm x 10 mm).

texture geometry	texture information	periodicity / mm	width / mm	depth / µm	area density	volume / mm^3
S1	patterned area: 7 x 7 mm^2	/	7	36.68 ± 5.67	0.245	1.79
S2	10 lines (length 7 mm)	0.7	0.23 ± 0.01	33.54 ± 2.54	0.082	0.49
S3	10 x 10 lines (length 7 mm)	0.7	0.24 ± 0.01	39.13 ± 4.03	0.168	1.31
S4	10 x 10 dimples	0.7	0.26 ± 0.01	38.43 ± 5.45	0.022	0.17

As can be seen in Table II, all textures have a similar structural depth with a mean value of around 35 µm; the standard deviations of the structural depth are less than 15 % for all samples. The largest standard deviation can be found for the single pocket S1, which can be explained by the texturing strategy to produce this geometry. After coupling the laser system with the translation stage, a meander path (constant sliding velocity) was programmed and multiple loops were required to achieve the desired single pocket geometry with dimensions of 7 mm x 7 mm x 35 µm. The partial overlap of the different paths induced some deviations in the resulting depth. Using a comb path, the line-like texture S2 consisting of ten lines aligned parallel to the short axis was produced. In order to fabricate the cross-like texture S3, the line-like texture was rotated by 90° and a second line-like texture keeping all settings constant was superimposed. The larger standard deviation of the structural depth for this geometry results from the overlapping area of the individual line-like textures. For the dot-like texture S4, the number of laser pulses needed to obtain the desired structural depth was evaluated without moving the translation stage. After having produced an individual dimple,

the translation stage was moved and the next dimple produced. Apart from the structural depth, the periodicity was 0.7 mm for all textured samples. Additionally, the width (top width for the line- and cross-textures as well as diameter for the dot-texture) was about 0.24 mm. Consequently, the diameter of each dot was similar to the feature width of the line-like and cross-like textures. The adjusted area density of the line-, cross- and dot-like pattern fits well with values recommended by other authors [12]. In addition, the entire pocket volume of the surface textures has been provided.

3.2 Tribological results – Experiments

As a first indication of the relative performance of each texture, **Figure 8** presents the oil film thickness at the outlet (i.e. the minimum oil film thickness) obtained for all convergence ratios tested with each texture's position. Since the load-support performance of a pad critically depends on the convergence ratio, and a wide range of convergence ratios were tested (between 0.1 and 18), there is naturally a wide spread of film thickness values for each sample. However, there are clear shifts in the range measured between different textures and front/rear positioning.

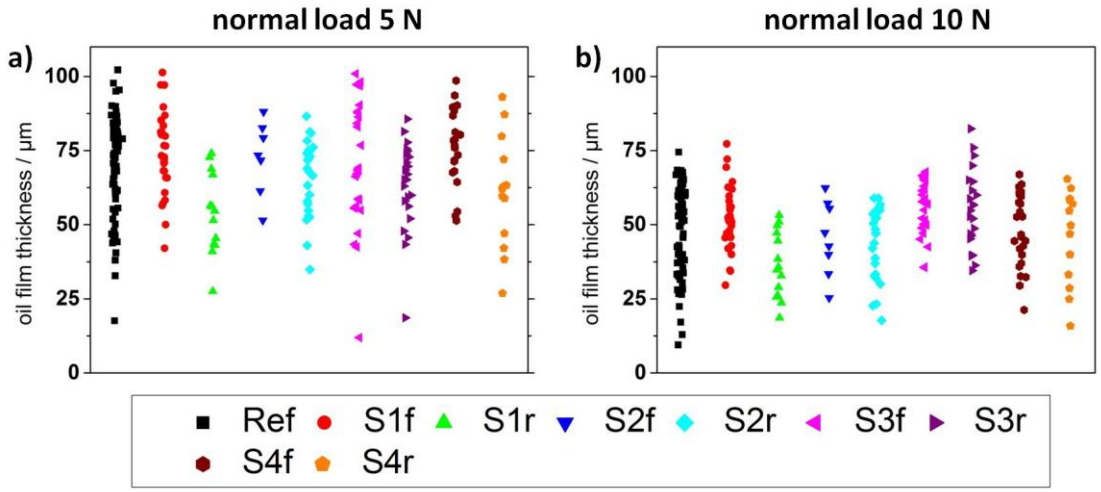

Figure 8: Summary of all oil film thicknesses measured by LIF irrespective of the adjusted convergence ratio for all texture geometries as well as normal loads of (a) 5 N and (b) 10 N.

Given that the process for setting and adjusting the convergence ratio was identical for each test, it can be expected that the range of results is related to configuration rather than any convergence bias. This is supported by a similar range of convergence ratios being measured for each configuration. Hence, the range of oil film thickness values can be considered as representative of the performance spread of a particular texture configuration (geometry and relative positive) across a span of convergence ratios.

Perhaps the most striking distinction between configurations is observed at 5 N load where there is a consistent shift in film thickness between the front and rear configuration of each texture. The texture at the rear consistently shows a lower-valued range of thicknesses than for the same texture at the front. The upper (better) end of the film-thickness range for the texture at the front is similar to the untextured reference, whilst a reduced film thickness is seen for texture at the rear. For a normal load of 10 N, this pattern is less consistent, and the films are naturally thinner than for the lower load. But again, there is a pronounced shift in the ranges for the single pocket with the texture at front (S1f) being significantly better than at the rear. This is in good agreement with the hydrodynamic lubrication theory if the texture is considered to act similar to a Rayleigh step. According to Olver et al. [44], a single pocket close to the oil inlet can lead to "inlet suction" thus increasing the oil film thickness and load support.

For the line-like texture with parallel grooves perpendicular to the sliding direction (S2), a reduction in the oil film thickness occurs irrespective of the normal load and relative position. A positive effect coming from a pressure build-up due to the perpendicular alignment of the

texture with respect to the flow direction of the oil seems to be overcompensated by possible side leakages [30, 32].

Regarding the dot-like textures (S4) under some experimental conditions, the maximum oil film thickness is comparable to the values observed for the polished reference. However, in general, this geometry produces lower film thicknesses (worse performance) than the reference. The reduced performance can be well correlated with the low area density and pocket volume (Table II).

The cross-like texture (S3) leads to similar or even slightly increased values for the maximum oil film thickness. For this geometry, two positive effects need to be considered. On the one hand, the lines oriented perpendicular to the oil flow induce an additional hydrodynamic pressure. On the other hand, lines that are parallel increase the oil volume (refer to the pocket volume summarized in Table II) transported in the convergence gap, which, in turn, increases the oil film thickness [30, 32].

The friction measured for each texture configuration is presented **Figure 9**, again with all convergence ratios included to help identify the spread of performance.

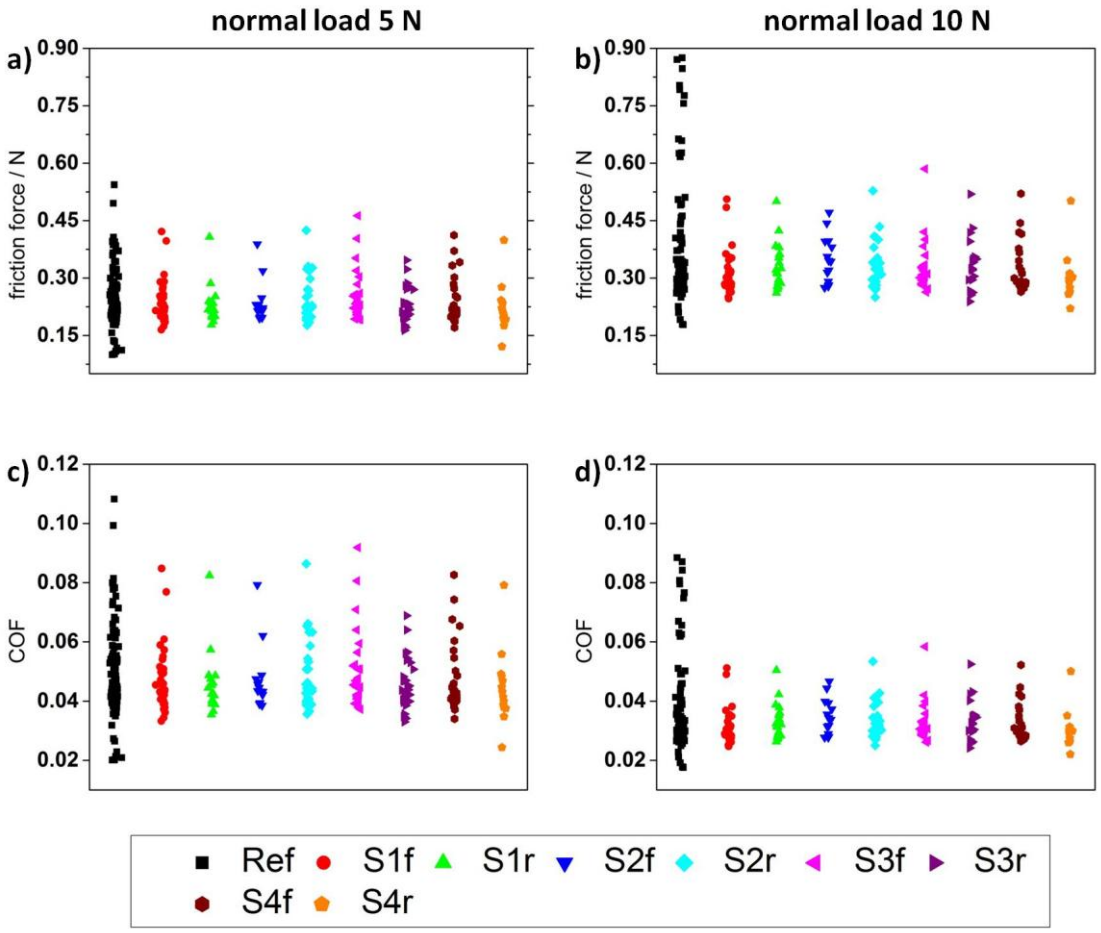

Figure 9: Summary of the measured friction force (a and b) and COF (c and d) for all tested samples, normal loads and convergence ratios.

For the case of friction, there is little difference between any of the texture designs or positions that can be extracted from the statistical spread. But all textures show a range of reduced extent and lower mean than the plain reference. The maximum friction reduction observed for the textures is around 40 % at 10 N, although the average reduction is substantially less. At 5 N load, there is a smaller but still observable reduction in friction. But it must also be recognised that, at both normal loads, the lowest friction case is for the plain, untextured sample. Potentially, it is at the less-optimal convergence ratios that the texture begins to become of most use. The lack of a similar effect for the oil film thickness values

suggests that it may, in fact, be a reduction in shear rate at the texture that contributes more to an improved frictional performance than any impact on an overall film thickness through load support enhancement. In this way, the greater gap between surfaces within the textured area creates a reduced shear-strain rate in the oil over these areas; with hydrodynamic friction being due to viscous forces associated with this shear, the reduced shear rate over a large proportion of the sample surface can significantly lower friction.

In these previous results, data at all convergence ratios have been agglomerated for each configuration. Given the critical nature of convergence in hydrodynamic lubrication, this may appear to degrade the value of the observations; yet in some ways, this actually provides a more valuable summary of the *practical* performance of each texture. In many real applications, the precise control of convergence is impossible or impractical to achieve, and surfaces are likely to experience a range of convergence ratios during operation (due to speed or load fluctuations). Consideration of the texture performance through a range of convergence ratios is, therefore, a necessary aspect in applying texture in applications. Nevertheless, to understand the mechanisms and details of the texture performance, a numerical evaluation taking into account the convergence ratio is needed.

3.3 Tribological results – Simulations

Numerical simulations for each texture configuration were run for a range of convergence ratios corresponding to the experiments (**Figure 10**). The convergence ratio is defined as $K = \left(\frac{h_{inlet}}{h_{outlet}} - 1\right)$ with h_{inlet} and h_{outlet} being the oil film thickness at the inlet and outlet, respectively.

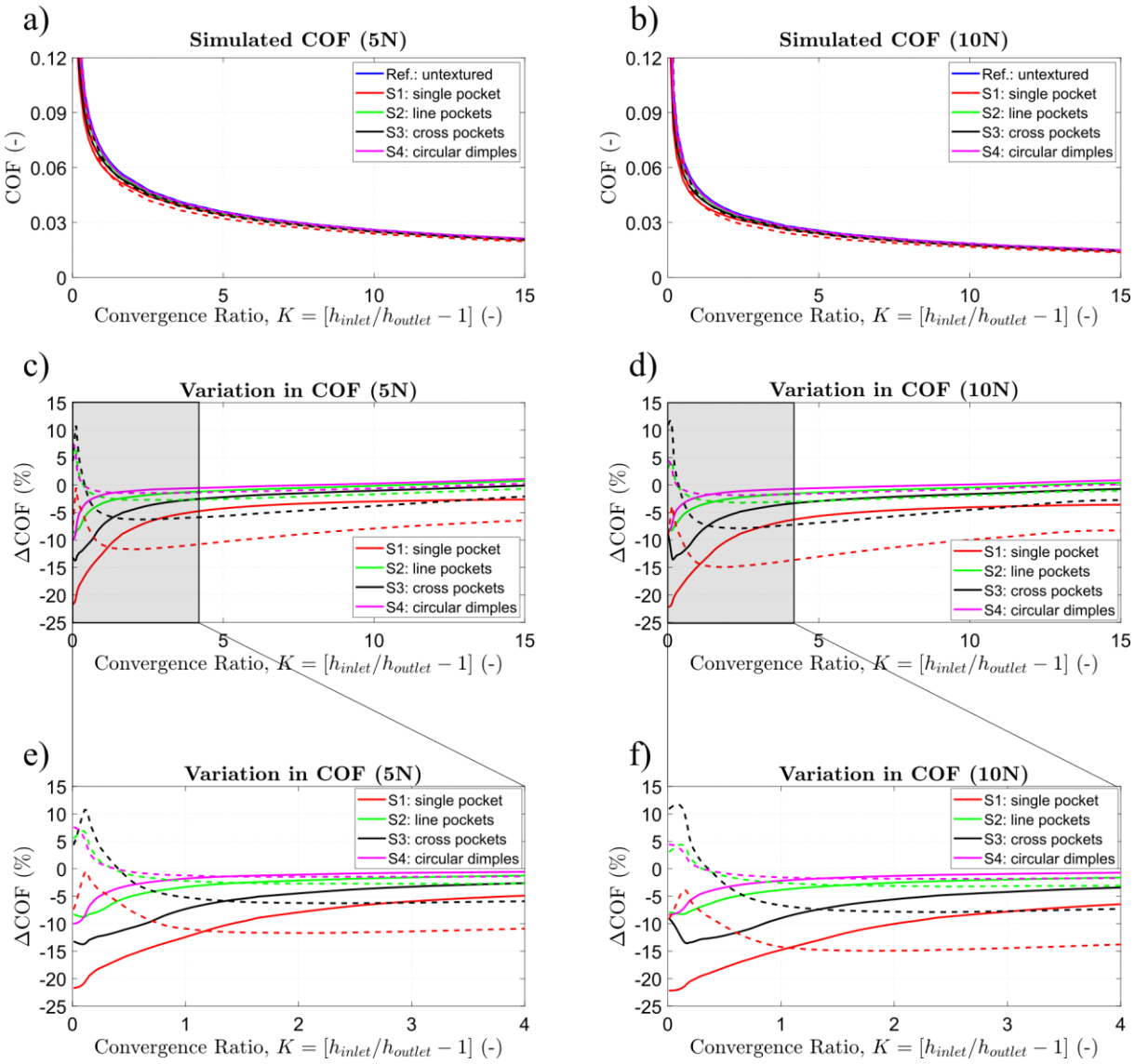

Figure 10: Simulated COF (a and b) and its variation (ΔCOF) with respect to the untextured reference (c-f) as a function of the convergence ratio for both normal loads. Solid lines: texture located at the inlet. Dashed lines: texture located at the outlet.

Figures 10 a and 10 b show the COF as a function of the convergence ratio, for each texture configuration at 5 and 10 N loads, respectively. There are only small differences in COF and these differences are clarified in Figure 10 c and d, which show the relative change in COF (ΔCOF) compared to the untextured references. Figures 10 e and 10 f show a close-up of the same relative change (ΔCOF) at low convergence ratios. Notice that the single pocket S1

seems to be one of the better performing designs, with improvements of up to 20 % at low convergence ratios and 5-15 % at higher values, and is the only pattern that provides a reduction in COF for all K values when located at the outlet. All other textures located at the outlet led to an increase of the friction coefficient ($\Delta COF > 0$) for $0.01 < K < 0.5$. In contrast, for the same range of convergence ratios ($0.01 < K < 0.5$), all textures at the inlet yielded considerable friction reductions ($\Delta COF < 0$) of up to 10-20 %, especially the single pocket (S1) and cross-like texture (S3).

These results can be understood better by also examining the effects on pressure distribution and film thickness. **Figures 11 and 12** show pressure distributions for each texture configuration at low (~ 0.3) and high (~ 8) convergence ratios, respectively, alongside the minimum oil film thickness (MOFT) and change in COF (ΔCOF) with respect to the untextured reference.

From the results presented in Figure 10, 11 and 12, it is seen that, for many of the textures, the performance is better with the texture at the *inlet* for low convergence ratios, switching to better performance with texture at the *outlet* at higher convergence ratios. This can be explained by considering two possible factors that can contribute to friction coefficient reduction: i) a load support enhancement, and ii) a localized film thickness increase purely due to the presence of the pockets. At low convergences, the texture at the inlet provides a boost to hydrodynamic load support, corresponding to lower overall friction coefficients, and texture at the rear *reduces* load support, corresponding to higher friction coefficients. Hence the observations at $K < 1$. On the other hand, at high convergence ratios, the texture has little effect on load support and average film thickness – and so it is the localised increase of film thickness within the pocket that matters. This makes a proportionally bigger impact at the rear, where the reference plane oil film thickness is lowest.

This is backed up by results in Figures 11 and 12, which, for the low convergence cases, show a minimum oil film thickness of 32.3 μm for the untextured sample, compared to 36.6 μm with the single pocket at front and only 29.5 μm for the single pocket at rear. Yet at the high convergence ratios, the film thicknesses are more similar (30.7 μm, 30.8 μm and 29.2 μm).

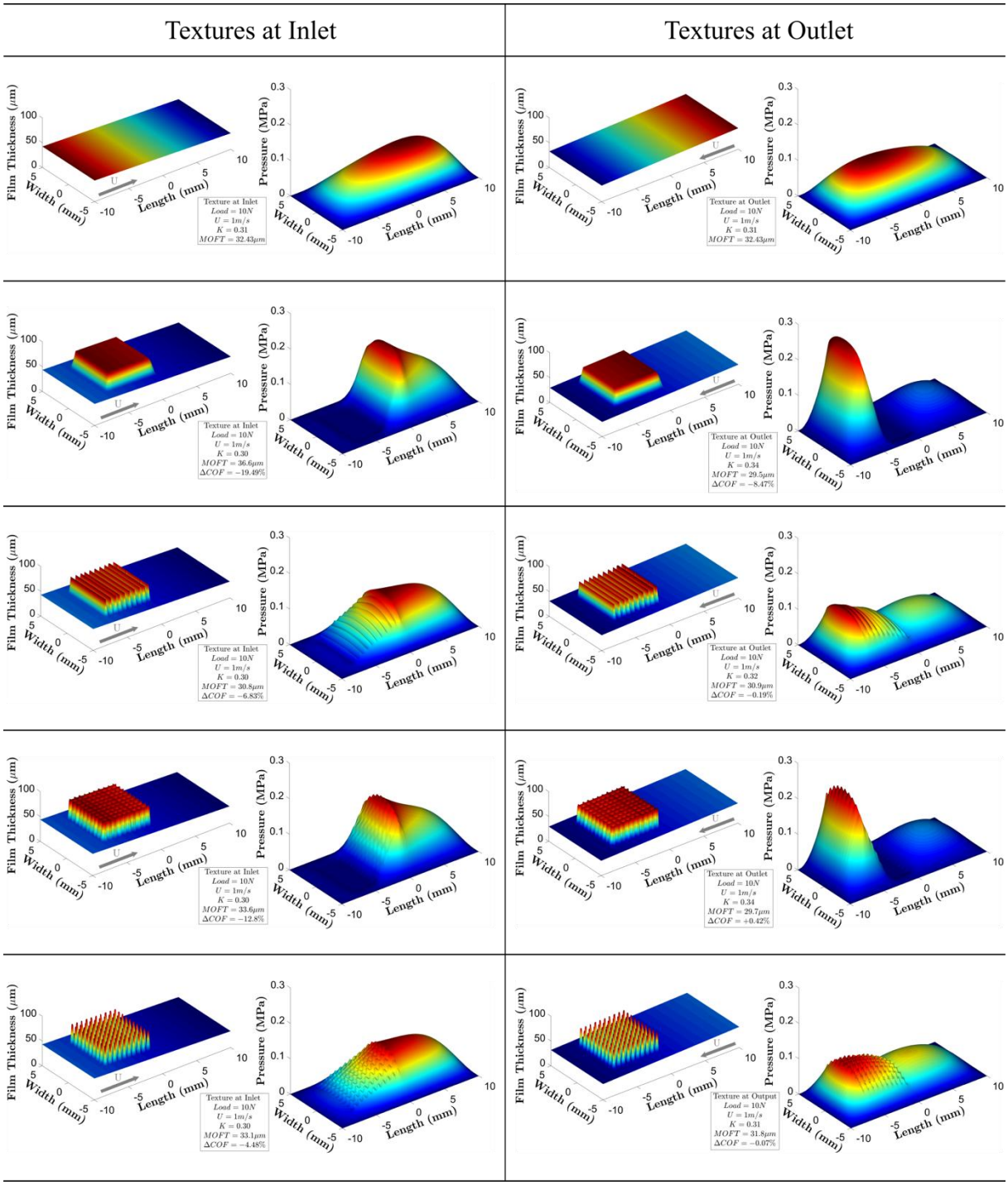

Figure 11: Fluid pressure distributions for all textures at the inlet (left) and outlet (right). The convergence ratio was about 0.3 and the normal load 10 N. The reader is referred to the video animations provided as a supplementary material in the online version of this article, which show the variations of the fluid pressure fields and the film fraction cavitation parameter distributions for all surface textures and convergence ratios simulated. It is important to highlight that the pressure distributions for a normal load of 5N follow the same trends.

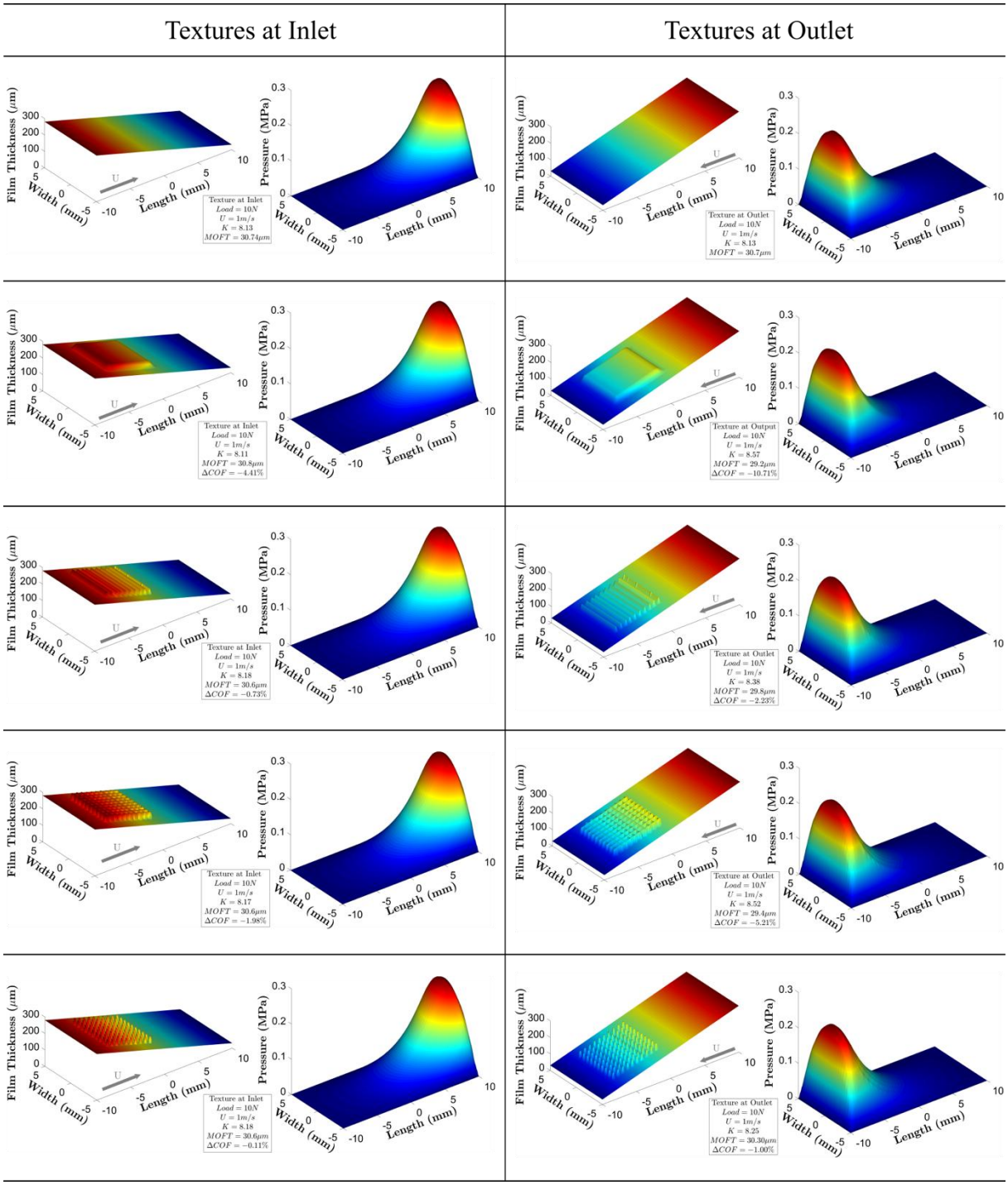

Figure 12: Fluid pressure distributions for all textures at the inlet (left) and outlet (right). The convergence ratio was about 8.2 and the normal load 10 N. The reader is referred to the video animations provided as a supplementary material in the online version of this article, which show the variations of the fluid pressure fields and the film fraction cavitation parameter distributions for all surface textures and convergence ratios simulated. It is important to highlight that the pressure distributions for a normal load of 5N follow the same trends.

Note that at high convergence ratios, the single pocket at the rear (S1r) actually produces a *lower* minimum film thickness, which would suggest higher friction; however, the opposite is true and friction is in fact reduced since the friction reduction due to the reduced shear stress within the textured area is more effective for the texture at the (lower) rear.

The pressure distribution for all cases is very similar at high convergence ratios, and all minimum oil film thickness values are in the narrow range of 29.2 to 30.8 µm. Texture has little effect on load support at high convergence ratios [13]. But at low convergence, there is a dramatic difference in pressure distribution between the reference and each different texture configuration, giving a greater spread of film thicknesses (29.5 to 36.6 µm).

Based upon Figure 10, the single pocket (S1r) and cross-like texture at rear (S3r), and single pocket at front (S1f) appear to show low friction for the majority of the convergence range. This is not apparent in the experimental results of Figure 8. Exploring this further, **Figure 13** shows the experimental COF results alongside the numerical simulation results, with the experimentally measured convergence ratios being used. The experimental results show good overall agreement with the numerical values, particularly at lower convergence ratios ($K < 5$). For higher convergence ratios, there is some deviation from predicted results, with the experimental values plateauing at around 0.04 (5 N) and 0.03 (10 N).

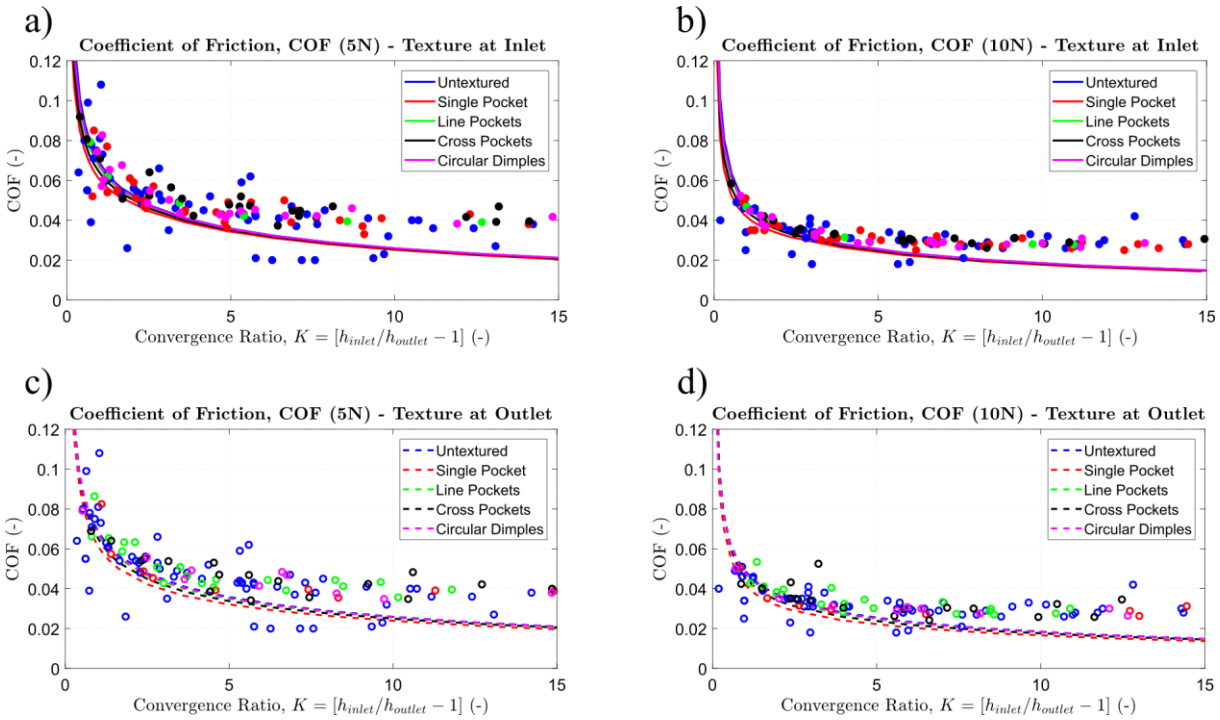

Figure 13: Comparison between the simulated (lines) and experimental (dots) data for the COF as a function of the convergence ratio. Solid lines and filled dots: textures at the inlet (a and b). Dashed lines and hollowed dots: textures at the outlet (c and d).

Figure 14 shows a similar comparison for the minimum film thickness measured and numerically predicted.

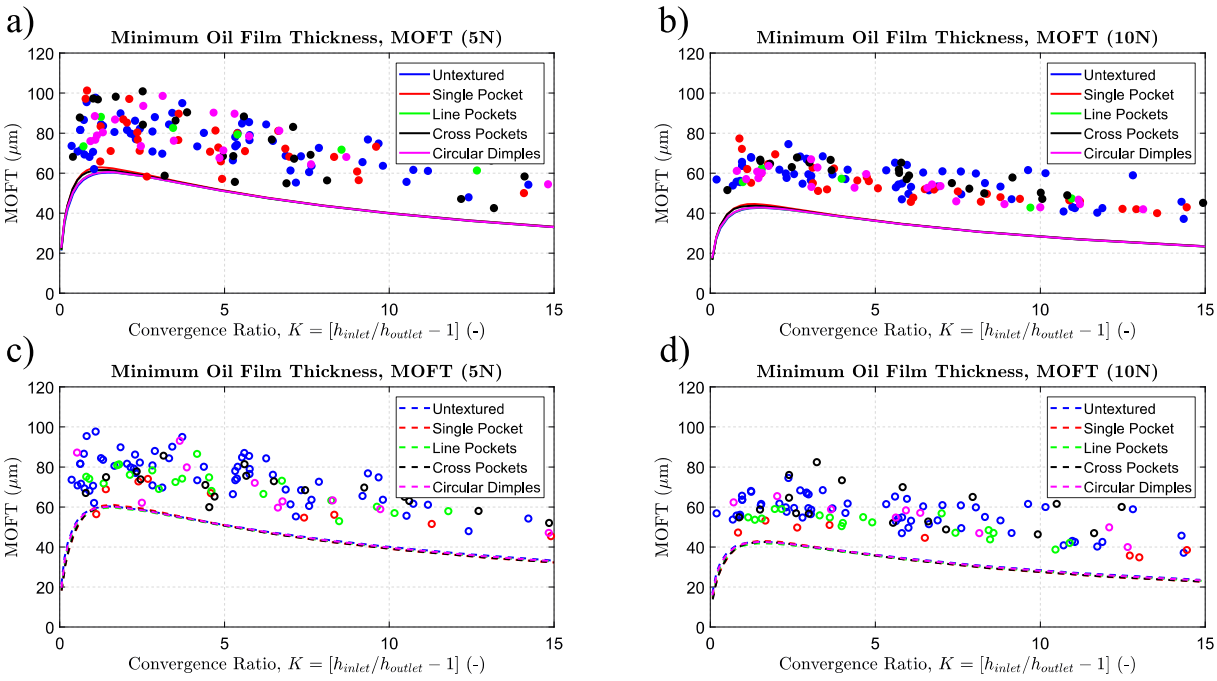

Figure 14: Comparison between the simulated (lines) and experimental (dots) data for the minimum film thickness (outlet) as a function of the convergence ratio. Solid lines and filled dots: textures at the inlet (a and b). Dashed lines and hollowed dots: textures at the outlet (c and d).

While the experimental results follow the same trend as the numerical results, there is a constant shift to higher film thickness values and a large scatter. There are several factors that potentially contribute to the differences and scatter observed. Firstly, the resolution of the LIF system begins to diminish at film thicknesses above 60 µm, leading to inaccuracies in convergence measurement as well as film thickness. The calibration process is also susceptible to a constant offset error, due to assumptions made for the calibration wedge shape. Moreover, the variation in sliding speed across the width of the pad (due to the varying radius on the rotating disc) is likely to lead to a deviation from the numerically predicted results. This variation can also contribute to a pad that is not perfectly aligned to the disc surface in the non-sliding direction – indeed this is possible even without such velocity variations because of frictional damping within the alignment pivot of the sample holder.

These factors all contribute to the great difficulty in achieving high experimental accuracy capable of quantitative comparisons with numerical results. Nevertheless, the experimental results obtained do support the conclusion that the textures can act to reduce friction across a full range of convergence ratios, and both the film thickness experimental and numerical results suggest this can be due to both load support enhancement at low convergence, and shear rate reduction at any convergence value.

4. Conclusions

This work used a carefully designed experimental set-up to assess the frictional performance of textured converging bearings under full-film lubrication for different convergence ratios. All tests were carried out under conditions resulting in very thick oil films (up to 100 micrometres), for which the literature currently reports small benefits of surface texturing. Both texture geometry and location in relation to lubricant entrainment were investigated. The experimental data were compared with numerical simulations based upon the solution of the Reynolds equation considering the $p - \theta$ Elrod-Adams mass-conserving cavitation model to examine the underlying lubrication mechanisms.

Based upon the results presented, the following conclusions can be drawn:

- The experimental investigation of the textures across a wide range of convergence ratios demonstrated that surface textures can have beneficial effects on the resulting COF at these high film thicknesses. Despite some scatter in the experimental results, there were identifiable differences in the texture's performance. In this context, the large single pocket and the cross-like texture showed the most significant impact.

- For a normal load of 5 N, a consistent shift in film thickness between the front and rear configuration of each texture was found. The texture at the rear consistently showed a lower-valued range of thicknesses, which underlines the importance of the texture's location.
- For high convergence ratios, numerical results suggested that most texture geometries and locations are beneficial. A significant COF reduction of up to 10 - 15 % was identified for the large single pocket and cross-like texture at the oil outlet.
- For low convergence ratios, numerical results also indicated that the texture location was critical – nearly all textures located at the outlet (except for the single pocket) led to an increase of the COF and all textures at the inlet yielded considerable friction reduction (up to 10 - 20 %). Considering the COF, there was a good overall agreement between numerical and experimental data, especially for low convergence ratios.
- Studying the effect of surface texturing on the resulting film thickness and friction force over a wide range of convergence ratios can provide valuable information about the *practical* performance of each texture. Bearing in mind that, in many real applications, the precise control of convergence is rather impossible, surfaces are likely to experience a wide range of convergence ratios during operation. Consideration of the texture performance through a range of convergence ratios can be considered as a necessary aspect in applying texture in applications.

5. Acknowledgements

The present work is supported by funding from the Deutsche Forschungsgemeinschaft in the priority program SPP 1551 "Resource efficient design elements" (DFG, project: MU 959/27-

1/2). The EU funding for the project AME-Lab (European Regional Development Fund C/4-EFRE-13/2009/Br) is gratefully acknowledged. Special thanks go to L. Reinert and B. Lechthaler for the help with the sample preparation.

6. References

[1] Bruzzone AAG, Costa HL, Lonardo PM, Lucca DA. Advances in engineered surfaces for functional performance. CIRP Ann Manuf Technol 2008;57:750-69. https://doi.org/10.1016/j.cirp.2008.09.003.

[2] Holmberg K, Andersson P, Erdemir A. Global energy consumption due to friction in passenger cars. Tribol Int 2012:47:221-34. https://doi.org/10.1016/j.triboint.2011.11.022.

[3] Holmberg K, Erdemir A. Influence of tribology on global energy consumption, costs and emissions. Friction 2017;5:263-84. https://doi.org/10.1007/s40544-017-0183-5.

[4] Martz LS. Preliminary report of developments in interrupted surface finishes. Proc Inst Mech Eng 1949;161:1-9. https://doi.org/10.1243/PIME_PROC_1949_161_007_02.

[5] Becker EP, Ludema KC. A qualitative empirical model of cylinder bore wear. Wear 1999;225-229:387-404. https://doi.org/10.1016/S0043-1648(98)00369-X.

[6] Hamilton DB, Walowit JA, Allen CM. A theory of lubrication by micro-irregularities. J Basic Eng - Trans ASME 1966:177-85. https://doi:10.1115/1.3645799.

[7] Anno JN, Walowit JA, Allen CM. Load support and leakage from microasperity-lubricated face seals. J Lubrication Tech 1969:726-31. https://doi:10.1115/1.3555030.

[8] Reynolds O. On the Theory of Lubrication and Its Application to Mr. Beauchamp Tower's Experiments, Including an Experimental Determination of the Viscosity of Olive Oil. Phil Trans R Soc Lond 1886;40:191-203. https://doi.org/10.1098/rstl.1886.0005.

[9] Findlay JA. Cavitation in mechanical seals. J Lubrication Tech 1968;April:356-64. https://doi:10.1115/1.3601569.

[10] Wang X, Kato K, Adachi K, Aizawa K. The effect of laser texturing of SiC surface on the critical load for the transition of water lubrication mode from hydrodynamic to mixed. Tribol Int 2001;34:703-11. https://doi.org/10.1016/S0301-679X(01)00063-9.

[11] Gropper D, Wang L, Harvey TJ. Hydrodynamic lubrication of textured surfaces: A review of modeling techniques and key findings. Tribol Int 2016;95:509-29. https://doi.org/10.1016/j.triboint.2015.10.009.

[12] Gachot C, Rosenkranz A, Hsu SM, Costa HL. A critical assessment of surface texturing for friction and wear improvement. Wear 2017;372–373:21-41. https://doi.org/10.1016/j.wear.2016.11.020.

[13] Fowell MT, Medina S, Olver AV, Spikes HA, Pegg IG. Parametric study of texturing in convergent bearings. Tribol Int 2012;52:7-16. https://doi.org/10.1016/j.triboint.2012.02.013.

[14] Costa HL, Hutchings IM. Hydrodynamic lubrication of textured steel surfaces under reciprocating sliding conditions. Tribol Int 2007;40:1227–38. https://doi.org/10.1016/j.triboint.2007.01.014.

[15] Vladescu SC, Olver AV, Pegg IG, Reddyhoff T. The effects of surface texture in reciprocating contacts – An experimental study. Tribol Int 2015;82, Part A:28-42. https://doi.org/10.1016/j.triboint.2014.09.015.

[16] Vladescu SC, Medina S, Olver AV, Pegg IG, Reddyhoff T. Lubricant film thickness and friction force measurements in a laser surface textured reciprocating line contact simulating the piston ring–liner pairing. Tribol Int 2016;98:317-29. https://doi.org/10.1016/j.triboint.2016.02.026.

[17] Lu P, Wood RJ, Gee MG, Wang L, Pfleging W. The use of anisotropic texturing for control of directional friction. Tribol. Int. 2017; 113:169-81. https://doi.org/10.1016/j.triboint.2016.02.026.

[18] Lu P, Wood RJ, Gee MG, Wang L, Pfleging W. A Novel Surface Texture Shape for Directional Friction Control. Tribol Lett 2018;66:51. https://doi.org/10.1007/s11249-018-0995-0.

[19] Ronen A, Etsion I, Kligerman Y. Friction-reducing surface-texturing in reciprocating automotive components. Tribol Trans 2001;44:359-66. https://doi.org/10.1080/10402000108982468.

[20] Burstein L, Ingman D. Pore ensemble statistics in application to lubrication under reciprocating motion. Tribol Trans 2002;43:205-12. https://doi.org/10.1080/10402000008982330.

[21] Ausas RF, Jai M, Buscaglia GC. A Mass-Conserving Algorithm for Dynamical Lubrication Problems With Cavitation. J Tribol 2009;131. https://doi:10.1115/1.3142903.

[22] Dobrica MB, Fillon M, Pascovici MD, Cicone T. Optimizing surface texture for hydrodynamic lubricated contacts using a mass-conserving numerical approach. Proc Inst Mech Eng J 2010;224:737-50. https://doi.org/10.1243/13506501JET673.

[23] Checo HM, Jaramillo A, Jai M, Buscaglia GC. Texture-induced cavitation bubbles and friction reduction in the Elrod–Adams model. Proc Inst Mech Eng J 2015;229:478-92. https://doi.org/10.1177%2F1350650114550012.

[24] Checo HM, Ausas RF, Jai M, Cadalen J-P, Choukroun F, Buscaglia GC. Moving textures: Simulation of a ring sliding on a textured liner. Tribol Int 2014;72:131-42. https://doi.org/10.1016/j.triboint.2013.12.013.

[25] Rahmani R, Mirzaee I, Shirvani A, Shirvani H. An analytical approach for analysis and optimisation of slider bearings with infinite width parallel textures. Tribol Int 2010;43:1551-65. https://doi.org/10.1016/j.triboint.2010.02.016.

[26] Codrignani A, Frohnapfel B, Magagnato F, Schreiber P, Schneider J. Gumbsch P. Numerical and experimental investigation of texture shape and position in the macroscopic contact. Tribol Int 2018;122:46-57. https://doi.org/10.1016/j.triboint.2018.02.001.

[27] Nanbu T, Ren N, Yasuda Y, Zhu D, Wang QJ. Micro-textures in concentrated conformal-contact lubrication: Effects of texture bottom shape and surface relative motion. Tribol Lett 2008;29:241-52. https://doi.org/10.1007/s11249-008-9302-9.

[28] Brizmer V, Kligerman Y, Etsion I. A laser surface textured parallel thrust bearing. Tribol Trans 2003;46:397-403. https://doi.org/10.1080/10402000308982643.

[29] Yu H, Wang X, Zhou F. Geometric shape effects of surface texture on the generation of hydrodynamic pressure between conformal contacting surfaces. Tribol Lett 2010;37:123-30. https://doi.org/10.1007/s11249-009-9497-4.

[30] Yuan S, Huang W, Wang X. Orientation effects of micro-grooves on sliding surfaces. Tribol Int 2011;44:1047-54. https://doi.org/10.1016/j.triboint.2011.04.007.

[31] Yagi K, Sugimura J. Balancing Wedge Action: A Contribution of Textured Surface to Hydrodynamic Pressure Generation. Tribol Lett 2013;50:349-64. https://doi.org/10.1007/s11249-013-0132-z.

[32] Scaraggi M. Textured Surface Hydrodynamic Lubrication: Discussion. Tribol Lett 2012;48:375-91. https://doi.org/10.1007/s11249-012-0025-6.

[33] Sahlin F, Glavatskih SB, Almqvist Tr, Larsson R. Two-Dimensional CFD-Analysis of Micro-Patterned Surfaces in Hydrodynamic Lubrication. J Tribol 2005;127:96-102. https://doi.org/10.1115/1.1828067.

[34] Nolte S, Momma C, Jacobs H, Tünnermann A, Chichkov BN, Wellegehausen B, Welling H. Ablation of metals by ultrashort laser pulses. J Opt Soc Am B 1997;14:2716-22. https://doi.org/10.1364/JOSAB.14.002716.

[35] Berlman IB. Handbook of fluorescence spectra of aromatic molecules, Academic Press 1971.

[36] Tala-Ighil N, Fillon M, Maspeyrot P. Effect of textured area on the performances of a hydrodynamic journal bearing. Tribol Int 2011;44:211-9. https://doi.org/10.1016/j.triboint.2010.10.003.

[37] Arencibia RV, Souza CC, Costa HL, Piratelli A. Simplified model to estimate uncertainty in CMM. Journal of the Brazilian Society of Mechanical Sciences and Engineering. 2015;37:411-21. https://doi.org/10.1007/s40430-014-0157-8.

[38] Floberg L. Cavitation boundary conditions with regard to the number of streamers and tensile strength of the liquid. Cavitation and related phenomena in lubrication: 1st Leeds-Lyon Symposium on Tribology. Leeds1974.

[39] Elrod HG. A computer program for cavitation and starvation problems. Proc 1st Leeds-Lyon Symp on Trib (Cavitation and Related Phenomena in Lubrication). 1975;37.

[40] Profito FJ, Giacopini M, Zachariadis DC, Dini D. A General Finite Volume Method for the Solution of the Reynolds Lubrication Equation with a Mass-Conserving Cavitation Model. Tribol Lett 2015;60:18. https://doi.org/10.1007/s11249-015-0588-0.

[41] Kelley CT. Solving Nonlinear Equations with Newton's Method,: Society for Industrial and Applied Mathematics; 2003.

[42] Profito F, Vladescu SC, Reddyhoff T, Dini D. Experimental Validation of a Mixed-Lubrication Regime Model for Textured Piston-Ring-Liner Contacts. Materials Performance and Characterization 2017;6:112-29. https://doi.org/10.1520/MPC20160019.

[43] Profito FJ, Vladescu SC, Reddyhoff T, Dini D. Transient experimental and modelling studies of laser-textured micro-grooved surfaces with a focus on piston-ring cylinder liner contacts. Tribol Int 2017;113:125-36. https://doi.org/10.1016/j.triboint.2016.12.003.

[44] Olver AV, Fowell MT, Spikes HA, Pegg IG. 'Inlet suction', a load support mechanism in non-convergent, pocketed, hydrodynamic bearings. Proc Inst Mech Eng J 2006;220:105-8. https://doi.org/10.1243%2F13506501JET168.